Title	Post-buckling development in soft particulate composites
Author(s)	Chen, Dean; Xiang, Yuhai; Arora, Nitesh; Yao, Qi; Li, Jian; Rudykh, Stephan
Publication Date	2023-07-26
Publication Information	Chen, Dean, Xiang, Yuhai, Arora, Nitesh, Yao, Qi, Li, Jian, & Rudykh, Stephan. (2023). Post-buckling development in soft particulate composites. Composite Structures, 322, 117337. doi: https://doi.org/10.1016/j.compstruct.2023.117337
Publisher	Elsevier
Link to publisher's version	https://doi.org/10.1016/j.compstruct.2023.117337
Item record	http://hdl.handle.net/10379/17980
DOI	http://dx.doi.org/10.1016/j.compstruct.2023.117337

Post-buckling development in soft particulate composites

Dean Chen [a], Yuhai Xiang [b], Nitesh Arora [a], Qi Yao [a], Jian Li [c,d], Stephan Rudykh [a,e,*]

[a] *Department of Mechanical Engineering, University of Wisconsin–Madison, WI 53706, United States*
[b] *Department of Chemical Engineering and Materials Science, University of Minnesota, Minneapolis 55455, MN, United States*
[c] *Joint International Research Laboratory of Key Technology for Rail Traffic Safety, Central South University, Changsha 410075, China*
[d] *Department of Civil and Environmental Engineering, Massachusetts Institute of Technology, Cambridge, MA 02139, United States*
[e] *School of Mathematical and Statistical Sciences, University of Galway, University Road, Galway, Ireland*

ARTICLE INFO

ABSTRACT

In this paper, we investigate the post-buckling development of instability-induced patterns in soft particulate composites. Upon reaching the critical strain level, the composite experiences microstructural buckling. Interestingly, in the post-buckling regime, the initial buckling mode may evolve into different new patterns. These transformations are governed by the initial microstructure parameters. In particular, depending on the initial distance between the columns of inclusions, the initial instabilities may develop into (i) inclusion chains with a zigzag or wavy shapes, (ii) a combination of inclusion sets in different length scales, (iii) seemingly disordered inclusion sets, (iv) and structures with strictly doubled periodicity. The different post-buckling patterns are further characterized via the discrete Fourier transform (DFT) analysis. Our results also show that the initially formed post-buckling patterns can further evolve into rather complex new shapes beyond a simple amplification in deformation.

1. Introduction

Elastic instabilities can induce dramatic microstructure transformations in soft composites at various length scales. Such transformations can enable the design of materials with tunable and switchable properties such as tunable bandgaps[29,46,48,54,21,44], negative group velocity states[51,2], and negative Poisson's ratio and auxetic behavior[6,8,25,26,28,40].

The instability analysis has frequently employed the framework of small deformations superimposed on the finitely deformed state[42]. The onset of macroscopic or longwave instabilities can be identified through the loss of ellipticity analysis. In composite materials, the loss of ellipticity analysis requires evaluations of the tensor of elastic moduli, which can be calculated through numerical[7,19,18,17,44,11,5,39] or analytical[47] homogenization approaches. Alternatively, the loss of the ellipticity condition can be determined directly through phenomenological models[35–38,33–34,4,13,53,43]. However, the onset of the so-called microscopic instabilities, which develops at finite wavelengths, may precede the occurrence of longwave instabilities[16]. To predict the onset of microscopic instabilities and to determine the critical level of deformation and wavelength, the Bloch-Floquet analysis is typically employed[16,52,6,50]. Note that the longwave limit in the Bloch-

Floquet analysis is equivalent to the loss of ellipticity condition[16].

These methods have been effectively applied in the theoretical prediction of instabilities in various soft systems and have also been realized via experimental investigations. For fiber composites (FCs), Galich et al. [15] examined the influence of the periodic fiber distribution on instabilities and shear wave propagation in 3D fiber composites. Rudykh & Debotton [47] employed micromechanics-based homogenization to predict the macroscopic instabilities in transversely isotropic fiber composites. Li et al. [27] experimentally observed the transition of elastic instabilities in 3D-printed fiber composites from small wavelength wavy patterns to longwave modes. Through both simulations and experiments, Arora et al. [3] examined the influence of constituent material properties on buckling orientation in fiber composites.

Li et al. [31] observed in experiments the microscopic and macroscopic instabilities in 3D-printed layered materials. Arora et al. [1] considered the inhomogeneous interphases in 3D-printed soft laminates and examined their influence on composite stability. Slesarenko and Rudykh [49] utilized the visco-hyperelastic behavior [55,56]) to achieve tunable wavy patterns through variable strain rates. Li et al. [29] analyzed the elastic instability in compressible laminates, where the stabilizing effect of phase compressibility was reported. Li et al. [30] experimentally observed the formation of twinning microstructures in

soft laminates driven by instabilities.

For particulate composites, Triantafyllidis et al. [52] studied the microscopic or macroscopic instabilities in particulate composites with circular inclusions under combined in-plane loadings. The re-examination of this problem under similar combined in-plane loadings was conducted by Michel et al. [41], which compared the macroscopic stability of the composite with a random distribution of circular or elliptical inclusions. Li et al. [24] experimentally observed the formation of wavy chain patterns in soft particulate composites. Goshkoderia et al. [20] reported that the pattern formation in soft particulate composites could be controlled via magnetic fields. Recently, Chen et al. [10] employed the Bloch-Floquet analysis to examine the influence of inclusion distributions on instability characteristics in soft particulate composites, including the critical strain and wavelength. We note that the Bloch-Floquet analysis and the alternatives, such as the refined eigenvalue analysis [6], are linearized methods. The post-buckling analysis considers the nonlinearity in the post-buckling development, thus, providing additional information (potentially more accurate) about the development of instability patterns under large deformations.

2. Theoretical background

Consider a continuum body, where each point is identified with its position vector X in the reference (or undeformed) and x in the current (or deformed) configurations. The corresponding mapping function is $x = \chi(X, t)$, where t denotes the time. The deformation gradient is defined as $F = \partial x/\partial X$, and its determinant is $J \equiv \det F > 0$. Consider a hyperelastic material with a strain energy density function, $W(F)$, so that the first Piola-Kirchhoff stress tensor is

$$P = \frac{\partial W(F)}{\partial F}. \tag{1}$$

For an incompressible material, $J = 1$, Eq. (1) modifies as

$$P = \frac{\partial W(F)}{\partial F} - pF^{-T}, \tag{2}$$

where p is an unknown Lagrange multiplier.

The relationship between the Cauchy stress tensor (σ) and the first Piola-Kirchhoff stress can be expressed as $\sigma = J^{-1}PF^T$. In the absence of body forces, the equations of motion for quasi-static deformation can be written in the undeformed configuration as

$$\text{Div} P = 0. \tag{3}$$

The analysis of the onset of instability and the post-buckling development is implemented numerically in the finite element code, as discussed in the next section.

3. Numerical simulation

In the numerical simulation, we consider a 2D periodic particulate composite consisting of a rectangular primitive unit cell with a single circular stiff inclusion located at its center (as illustrated in Fig. 1). The dimensions of the primitive unit cell are defined by its width a and length b. The geometry of the unit cell can be fully determined using two parameters: the periodicity aspect ratio $\eta = a/b$ and the inclusion spacing ratio $\xi = d/b$, where d represents the diameter of the inclusion. The numerical analysis has been implemented in the finite element code in COMSOL Multiphysics 6.0.

To perform the post-buckling analysis, we construct a *representative volume element* (RVE) [6] with a large number ($N = 80$) of unit cells. The RVE is enclosed by four boundaries (AB, CD, AC, and BD), defined by nodes A, B, C, and D. We apply uniaxial compression *quasi-statically* via periodic boundary conditions imposed on the boundary pair $AB - CD$ and $AC - BD$ as

$$u_{src} - u_{dst} = (\overline{F} - I)(X|_{src} - X|_{dst}) = \overline{H}(X|_{src} - X|_{dst}), \tag{4}$$

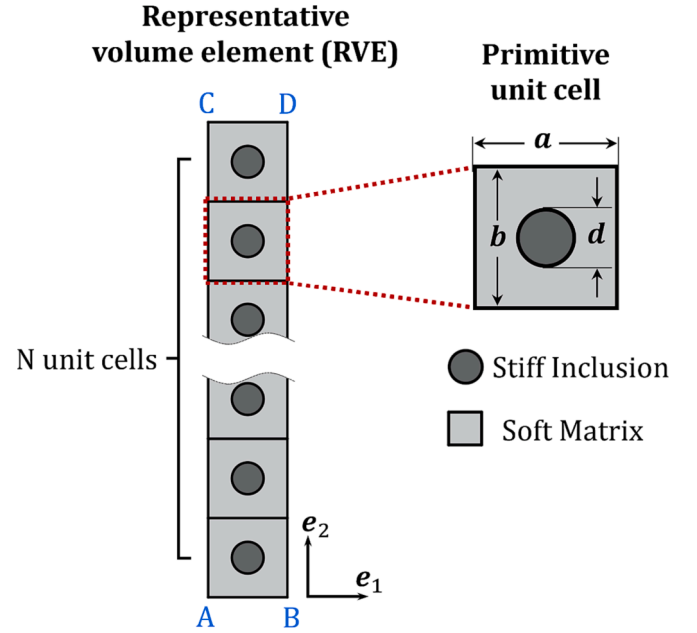**Fig. 1.** Schematic composite microstructure with stiff circular inclusions periodically distributed in soft matrices.

where u_{src} and u_{dst} represent the displacement of an arbitrary pair of points periodically located on the *source* and *destination* boundary of the boundary pair, respectively; $\overline{F}$ denotes the average deformation gradient, I denotes the identity tensor and $\overline{H} = \overline{F} - I$ denotes the average displacement gradient. We apply the in-plane unidirectional compression to the RVE in the direction of e_2 via the displacement gradient defined as

$$\overline{H} = (\lambda_1 - 1)e_1 \otimes e_1 + (\lambda_2 - 1)e_2 \otimes e_2, \tag{5}$$

where λ_1 and λ_2 are the principal stretch ratios in the direction of e_1 and e_2, respectively. The compressive loading level is prescribed via the average compressive strain $\varepsilon = 1 - \lambda_2$. λ_1 is defined via $\lambda_1\lambda_2 = 1$ according to the incompressibility of materials. In the post-buckling analysis, geometrical imperfections are introduced in terms of a small alternation of the shape and position of the stiff inclusions (the details are provided in Appendix C).

The stiff inclusion and soft matrix materials are described by the hyperelastic models with nearly incompressible neo-Hookean strain energy density function, namely,

$$W^{(r)} = \frac{\mu^{(r)}}{2}(I_1 - 3) + \frac{\kappa^{(r)}}{2}(J - 1)^2, \tag{6}$$

where $\mu^{(r)}$ is the initial shear modulus, $\kappa^{(r)}$ is the bulk modulus, and $I_1 = \text{tr} C$ is the first invariant of the right Cauchy-Green tensor $C = F^T F$. The superscript (r) indicates the properties of different material phases; for example, $(r) = (i)$ denotes the stiff inclusion phases, and $(r) = (m)$ denotes the soft matrix phases. We introduce the ratio $\Lambda = \kappa^{(r)}/\mu^{(r)}$ representing the material compressibility, and assign a high ratio, $\Lambda = 10^3$, to maintain a nearly incompressible behavior of the materials. We select the inclusion-to-matrix ratio of shear moduli $\mu^{(i)}/\mu^{(m)} = 10^3$. Therefore, stiff inclusions barely deform, and the deformation is mostly accommodated by the soft matrix.

4. Results and analysis

4.1. Analysis of post-buckling development

This section presents the post-buckling numerical calculation results and analysis. We start with an example of the particulate composite with

the spacing ratio $\xi = 0.6$ and periodicity aspect ratio $\eta = 2.1$. Fig. 2a shows the corresponding initial RVE at $\varepsilon = 0$. For a more compact illustration, only 40-unit cells of the RVE are displayed here and thereafter. We observe that the composite material maintains a straight column of inclusions until a critical strain level of $\varepsilon^{cr} = 0.233$ is reached. At this point the inclusion column experiences a sudden collapse and transforms into a wavy chain of inclusions. This can be observed in the deformed RVE shown in Fig. 2a, corresponding to $\varepsilon = 0.253$.

The onset of instability is identified by detecting the initialization of the inclusion column collapse. Specifically, the relative horizontal displacement between adjacent inclusions is monitored, and once it exceeds a small threshold value, the critical strain is identified (the detailed procedure is described in Appendix A). The corresponding critical strain identified through the post-buckling analysis is $\varepsilon^{cr} = 0.233$ (for the composite with $\xi = 0.6$ and $\eta = 2.1$); this value is in good agreement with the prediction of the Bloch-Floquet analysis, namely, $\varepsilon^{cr} = 0.2338$ [10]. In experiments, Li et al. [24] also observed the formation of the "wavy chain" pattern of inclusions. This pattern transformation, induced by elastic instabilities, is a result of the breaking of the composite's initial periodicity, characterized by the initial wavelength $L^0 = b$, and the emergence of a new periodicity, characterized by the critical wavelength $L^{cr} = [k^{cr}]^{-1}b$, where k^{cr} is the *normalized* critical wavenumber and $l^{cr} = [k^{cr}]^{-1}$ is the corresponding *normalized* critical wavelength. For simplicity, in this study, we illustrate the results in terms of the normalized critical values, such as k^{cr} and l^{cr}, and refer to them as the critical wavenumber and critical strain, respectively. It is

worth noting that the critical wavelength L^{cr} also represents the height of the smallest repeating unit of the post-buckling configuration, referred to as the "enlarged primitive cell" [10,6]. Let us examine the instability-induced pattern in the composite in the post-buckling regime, in particular, at a strain level exceeding the critical value, namely, $\varepsilon = 0.253$. First, repeating blocks of seven inclusions may be observed; that would correspond to the critical wavelength of $l^{cr} \approx 7$. However, a further inspection of the distribution of inclusions shows that the position (phase) of the corresponding inclusion within different blocks is slightly shifted. For example, the fourth inclusion (from the left) in blocks (3) and (4) shifts slightly downward in comparison to that in blocks (1) and (2). This deviation stems from the fact that the critical wavelength of the instability mode does not correspond to an integer number of initial primitive cells. In particular, according to our Bloch-Floquet analysis, the critical wavelength of this numerical case is predicted to be $l^{cr} \approx 6.89$. Therefore, in the post-buckling regime, the composite is unable to form a strictly periodic structure matching by critical wavelength, and is then forced to adapt a configuration with an integer wavelength $l^{cr} = 7$. This forced adaption, however, results in a somewhat frustrated distribution of inclusions and thus leads to the mismatch of inclusion centers in different inclusion blocks. This frustration brings about serious difficulty (sometimes makes it nearly impossible) in determining the actual size of the enlarged primitive cell. Therefore, a substitute method that circumvents this effect of the inclusion needs to be employed for the correct identification of the critical wavenumber. In our study, we introduced a standard post-processing
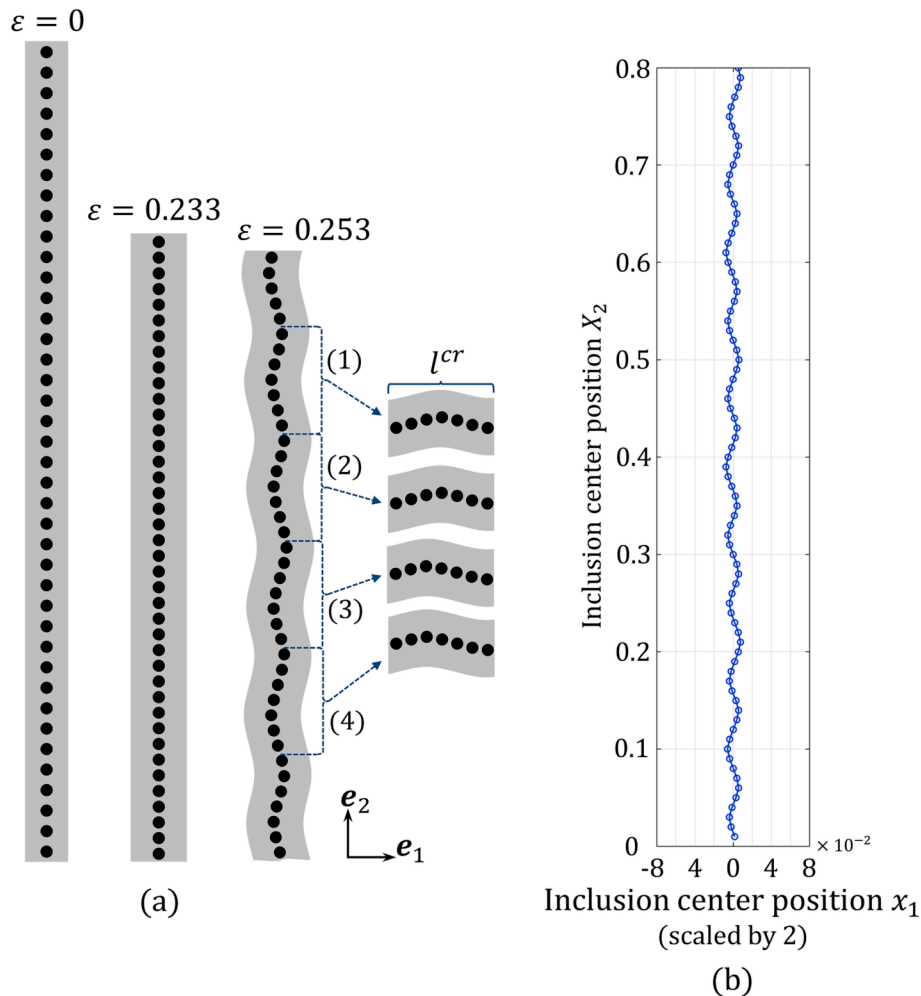

Fig. 2. (a) The deformation sequence under compressive strain level $\varepsilon = 0$, 0.233, and 0.253; initial geometric parameters are $\xi = 0.6$ and $\eta = 2.1$; (b) The position of inclusion centers in the deformed RVE.

method that characterizes the post-buckling structure obtained from FEA and then identifies the corresponding critical wavenumber. In the post-processing analysis, we track the position displacement of the inclusion centers, as the inclusion wavy chain is formed and developed in the post-buckling regime. This procedure is illustrated by a representation of the discrete wavy curve (connecting the centers of the stiff inclusions) in Fig. 2(b). The inclusion center connection curve is built by considering the horizontal displacement of the inclusion centers (in e_1 direction); the deformations of the stiff inclusions are neglected. Next, we apply a discrete Fourier transformation (DFT) on the obtained inclusion center point curve to find its wavenumber components. Given a discrete curve defined by the position of inclusions, namely, $\{x_n\} := x_1$, $x_2, x_3 \cdots, x_N$ in e_1 direction, the DFT utilizes a set of discrete harmonic curves based on the fundamental wavenumber $1/N$ to reassemble the discrete curve $\{x_n\}$, where N is the number of inclusions in the RVE, and the corresponding wavenumber of the K th harmonic curve is K/N. Through the discrete Fourier transformation, we obtain the dependence of the Fourier coefficient f_K on the corresponding component wavenumber $k = K/N$ by solving the linear equation system

$$x_n = \sum_{K=0}^{N-1} f_K \bullet e^{i2\pi \frac{K}{N} n}. \tag{7}$$

Finally, the DFT result is represented as a wavenumber spectrum $f_K = F(k)$, where f_K is Fourier coefficient and k is the component wavenumber ($k = 1/N, 2/N, ..., (N-1)/N, 1$).

Next, we illustrate the results of the DFT analysis in Fig. 3, showing the dependence of the Fourier coefficient f on component wavenumber $k = 0.0125, 0.025, ... 0.4875$ and 0.5, for fixed compressive strain levels (from 0.23 to 0.24). We observe that, below the critical strain level $\varepsilon^{cr} = 0.2338$, the composite maintains a straight column of inclusions, and correspondingly, we observe that all component wavenumbers are characterized by nearly zero Fourier coefficients. For example, in the green curve with circular markers corresponding to $\varepsilon = 0.233$ in Fig. 3, we observe a straight chain of inclusions in the composite; the corresponding DFT result is a horizontal line at zero values. However, after reaching the critical strain level ($\varepsilon^{cr} = 0.2338$), the inclusion column

suddenly collapses and transforms into a wavy chain. Correspondingly, a peak of the Fourier coefficient emerges at $k = 0.145$. This is illustrated by the yellow curve with square markers corresponding to $\varepsilon = 0.235$ in Fig. 3. We observe a peak in the curve at $k = 0.145$ as the corresponding post-buckling pattern develops a wavy chain. Next, with an increase in the compressive strain level, the post-buckling deformation develops further, and the amplitude of the wavy-chain pattern increases. Correspondingly, we observe that the peak Fourier coefficient (at $k = 0.145$) becomes more prominent. This is also reflected in the increase in the amplitude of the wavy-chain pattern (see, for example, the DFT results corresponding to the compressive strain increased from $\varepsilon = 0.2339$ to $\varepsilon = 0.24$). The peak point in DFT results corresponds to a component harmonic curve that dominates the post-buckling wavy chain pattern, and the corresponding wavenumber of this peak point ($k^{cr} = 0.145$) is then identified as the critical wavenumber. This identification method may be applied for post-buckling analysis of particulate composites to identify the critical wavenumber, including the scenario with the frustrating distribution of inclusions (without identifying the enlarged primitive cell). We note that the precision of the DFT analysis depends on the number of component wavenumbers scanned, which is also identical to the number of unit cells built in the RVE. Increasing the number of unit cells in the RVE can improve the accuracy of the wavenumber identification process. Our numerical results indicate that 80 unit cells are sufficient for obtaining the critical wavenumber accurately. The corresponding comparison of the DFT results obtained with different numbers of unit cells (from 20 to 200) in the RVE is given in Appendix B.

4.2. Transition of post-buckling patterns with periodicity aspect ratios

We start by examining the post-buckling development with various initial geometrical parameters of the periodic microstructure. Specifically, the periodicity aspect and spacing ratios are altered by modifying the width of the unit cell and the diameter of the inclusion, respectively, while the height of the unit cell keeps constant. First, we examine the composites with a high spacing ratio $\xi = 0.8$ (the inclusions are placed relatively close in the direction of compression) and various periodicity
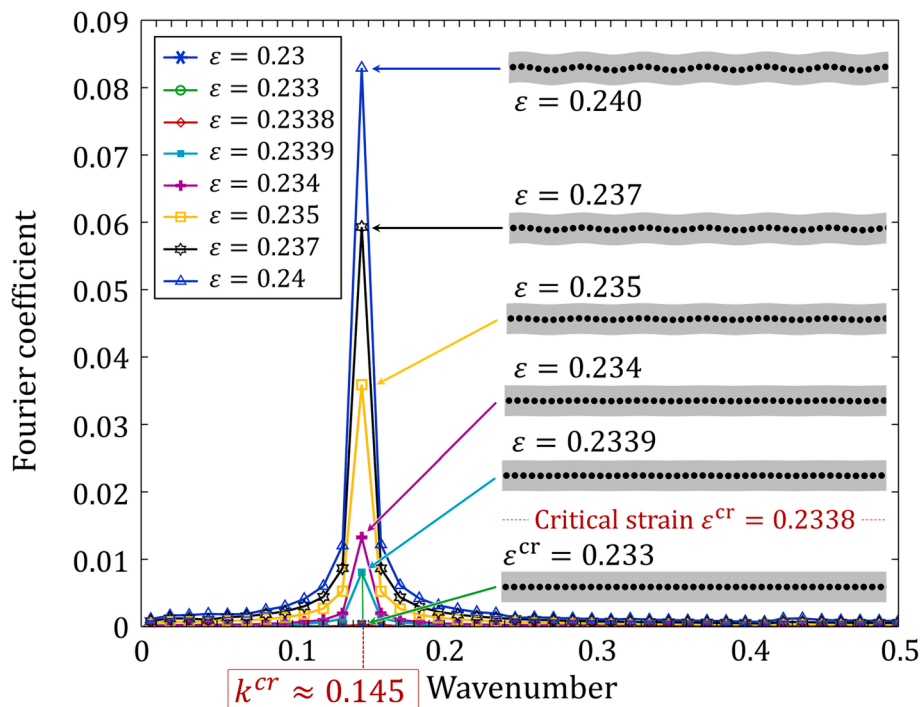

Fig. 3. The DFT analysis results of the post-buckling development for the composite with spacing ratio $\xi = 0.6$ and periodicity aspect ratio $\eta = 2.1$ at compressive strain $\varepsilon = 0.233$, $\varepsilon = 0.2339$, $\varepsilon = 0.234$, $\varepsilon = 0.235$, $\varepsilon = 0.237$, and $\varepsilon = 0.24$ with $N = 80$ number of unit cells built in the RVE.

aspect ratios. In the upper part of Fig. 4, the red curve shows the dependence of the critical wavenumber k^{cr} on the periodicity aspect ratio η predicted by Bloch-Floquet analysis (from $\eta = 2.5$ to $\eta = 8.0$) for the fixed spacing ratio $\xi = 0.8$. The corresponding DFT analysis results of the post-buckling pattern are overlayed on the curve plot for the composites with periodicity aspect ratio $\eta = 2.7, 3.0, 3.25, 3.5, 4.0, 4.75, 6.0,$ and 7.5, where the vertical axis is the wavenumber, and the horizontal value is the corresponding Fourier coefficient. The lower part of Fig. 4 includes the corresponding post-buckling patterns, showing inclusion center positions at higher strain levels (after the onset of instability). The criterion for selecting these strain levels is based on the relative displacement of the inclusion centers; specifically, the post-buckling structures attain the same value of the so-called average amount of shear. Appendix A describes the details of how this criterion is defined and applied.

In Fig. 4, we included the Bloch-Floquet prediction of k^{cr} (red curve); the Bloch-Floquet curve starts with the longwave instability ($k^{cr} \rightarrow 0$) and transits to a microscopic instability ($k^{cr} > 0$) as the periodicity aspect ratio increases (corresponding to the inclusion columns placed farther away from each other) beyond a threshold value $\eta^{th} \approx 2.95$. For the corresponding post-buckling patterns, we observe a single period of the zigzag chain pattern for every longwave instability mode (see, for example, the pattern in the lower part of Fig. 4 corresponding to $\eta = 2.7$), with the DFT analysis identifying a single peak of Fourier coefficient at $k^{cr} = 0.0125$ (corresponding to the critical wavelength $l^{cr} = 80$,

the height of the entire RVE). This is a result of the buckling wavelength being significantly larger than the characteristic size of the microstructure. Specifically, when a finite-sized RVE is used, only a single period of pattern with a critical wavelength corresponding to the height of the RVE will be observed in the cases of longwave instabilities; the peak of the DFT result will be found at the smallest wavenumber scanned, namely, the fundamental wavenumber $k = 1/N$. Similarly, if a larger number of unit cells in the RVE is used (for example, 200 cells), the critical wavelength will increase to $l^{cr} = 200$ and the corresponding critical wavenumber shifts down to $k = 1/200$.

For the microscopic instability modes ($k^{cr} > 0$), the corresponding critical wavelength is smaller than the height of RVE; hence, the wavy chain pattern emerges in the post-buckling regime. For example, for the patterns corresponding to $\eta = 3.0$, and $\eta = 3.25$ in the lower part of Fig. 4, the inclusion centers are observed in overall wavy distribution. The corresponding DFT results show a single peak emerging after the onset of instability, and the corresponding wavenumber values are close to those predicted via the Bloch-Floquet analysis. For instance, in the DFT result corresponding to $\eta = 3.0$ (in the upper part of Fig. 4), we observe a single peak of the Fourier coefficient at the wavenumber $k = 0.075$, and the corresponding Bloch-Floquet analysis prediction is $k^{cr} = 0.077$.

Next, we examine the post-buckling development in the composite with a relatively low spacing ratio $\xi = 0.3$ (the inclusions are placed relatively far away in the direction of compression) for various period-
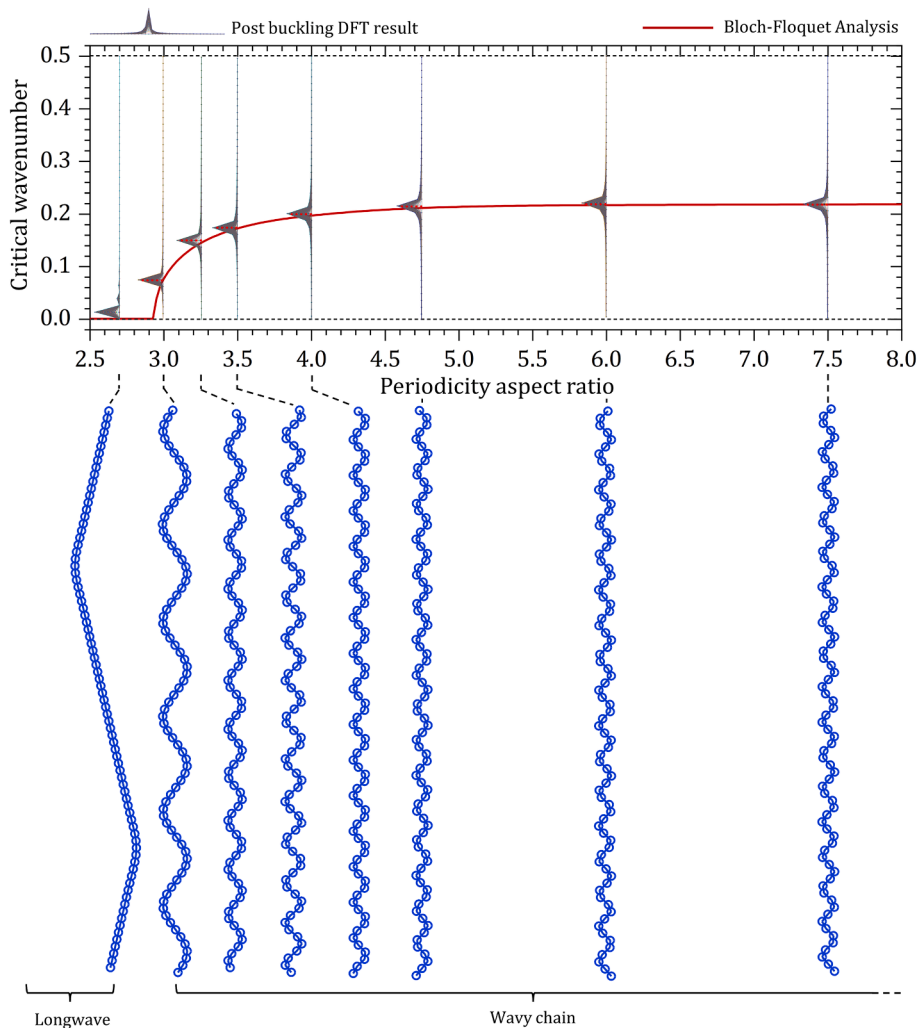

Fig. 4. Post-buckling patterns and the corresponding DFT results with fixed spacing ratio $\xi = 0.8$ and various periodicity aspect ratios (compared with the critical wavenumber predicted from the Bloch-Floquet analysis).

icity aspect ratios. In the upper part of Fig. 5, the Bloch-Floquet curve shows the dependence of the critical wavenumber k^{cr} on the periodicity aspect ratio η for a fixed inclusion spacing ratio $\xi = 0.3$. The corresponding DFT results of the post-buckling pattern are also overlaid on the curve for the composite with periodicity aspect ratios $\eta = $ 0.8, 0.9, 1.0, 1.04, 1.06, 1.1, 1.2, and 1.3. The lower part of Fig. 5 shows the corresponding post-buckling patterns. For this composite configuration, the Bloch-Floquet predicts the critical wavenumber with only binary values, namely, either $k^{cr} \to 0$ or $k^{cr} = 0.5$. The wavenumber starts with $k^{cr} \to 0$ in the initial ranges of the periodicity aspect ratio, and it jumps from $k^{cr} \to 0$ to $k^{cr} \to 0.5$ after a threshold value $\eta^{th} \approx 1.05$, without any intermediate wavenumber during the transition. In the post-buckling analysis, the zigzag chain pattern for the longwave instability mode develops (see, for example, the pattern in the lower part of Fig. 5 corresponding to $\eta = 1.0$), with single peak of Fourier coefficient at $k^{cr} = 0.0125$ in the DFT analysis. For the microscopic instability mode with $k^{cr} = 0.5$, the initial periodicity doubles (*exactly*) upon buckling, and we observe a repeating two-inclusion period in the post-buckling pattern, namely, the periodicity-doubling pattern (see, for example, the patterns in the lower part of Fig. 5 corresponding to $\eta = 1.2$). The DFT analysis also shows a single peak of the Fourier coefficient at the wavenumber $k = 0.5$, corresponding to the critical wavelength $l^{cr} = 2$. In our numerical results, only the "zigzag chain" and the periodicity doubling patterns were found for composites with $\xi = 0.3$. This binary result

holds true even in cases that are close to the threshold value of $\eta^{th} \approx 1.05$. For example, as shown in the lower part of Fig. 5, the post-buckling patterns for $\eta = 1.04$ and $\eta = 1.06$ exhibit zigzag chain and periodicity doubling patterns, correspondingly; no wavy chain patterns are observed.

Finally, we examine the post-buckling development of the composite with a moderate spacing ratio, namely, $\xi = 0.45$ and various periodicity aspect ratios. These composite configurations are characterized by a full evolution of critical wavenumber from the longwave ($k^{cr} \to 0$) to the periodicity-doubling mode ($k^{cr} = 0.5$) with an increase in the periodicity aspect ratio (corresponding to an increasing distance between inclusion columns). This is illustrated by the red curve in the upper part of Fig. 6, showing the dependence of (the Bloch-Floquet predicted) critical wavenumber k^{cr} on the periodicity aspect ratio η for fixed inclusion spacing ratio $\xi = 0.45$. The lower part of the figure shows the corresponding post-buckling patterns. In the lower part of Fig. 6, we observe an overall transition of the post-buckling patterns from a zigzag chain (for example, the pattern corresponding to $\eta < 1.46$) to the periodicity doubling pattern (for example, the pattern corresponding to $\eta > 2.18$). During the transition range (from $\eta = 1.46$ to $\eta = 2.18$), the post-buckling development starts with the wavy chain pattern corresponding to a relatively small critical wavenumber (see, for example, the cases corresponding to $k^{cr} = 1.5$ and $k^{cr} = 1.6$ in Fig. 6). However, as the critical wavenumber increases beyond $k^{cr} \approx 0.25$, we observe a

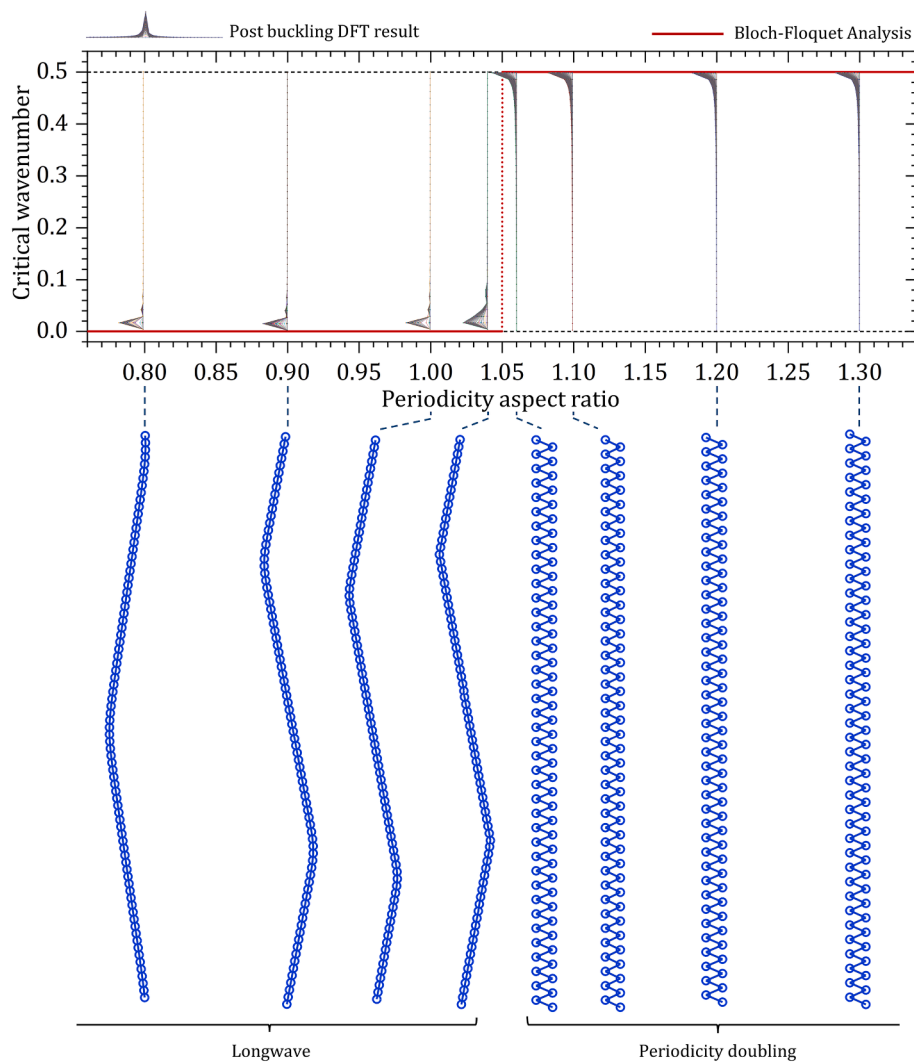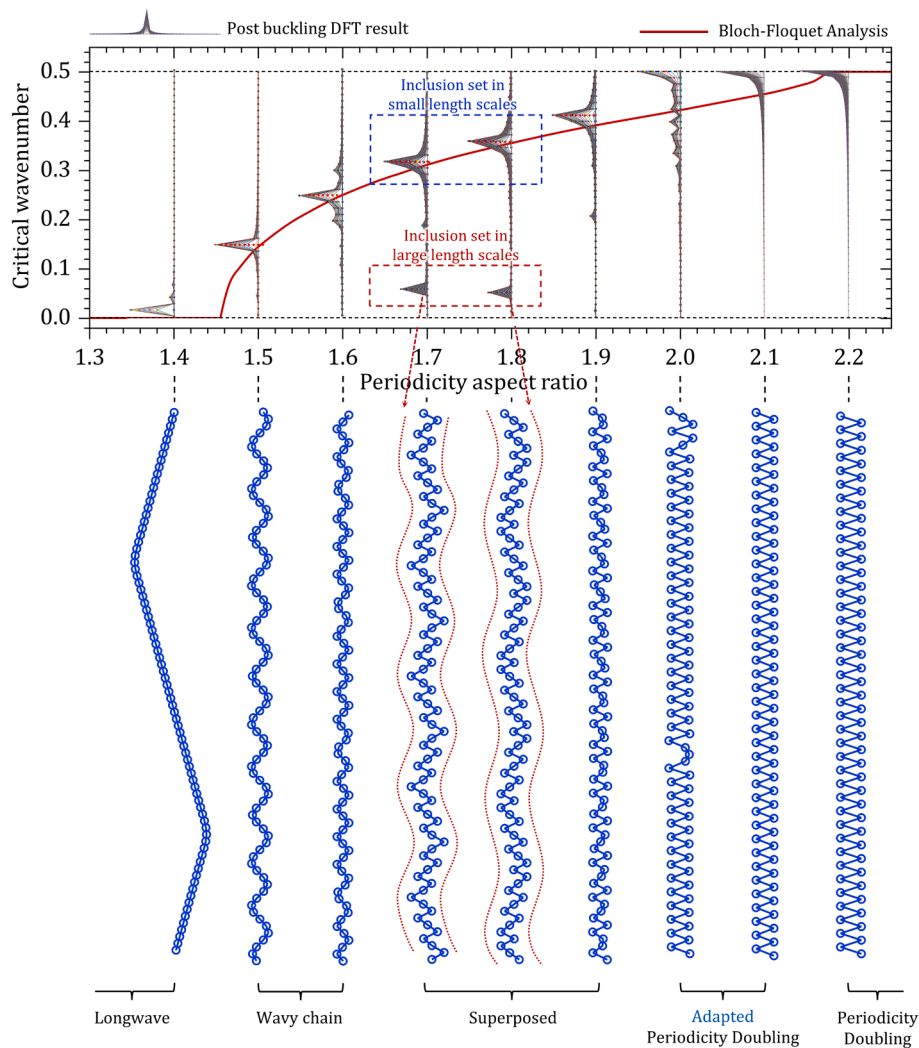

Fig. 5. Post-buckling patterns and the corresponding DFT results with fixed spacing ratio $\xi = 0.3$ and various periodicity aspect ratios (in comparison with the critical wavenumber predicted from Bloch-Floquet analysis).

Fig. 6. Post-buckling patterns and the corresponding DFT results with fixed spacing ratio $\xi = 0.45$ and various periodicity aspect ratios (compared with the critical wavenumber predicted from Bloch-Floquet analysis).

significant change in the post-buckling shapes (see the patterns corresponding to $\eta = 1.7$ and $\eta = 1.8$ in Fig. 6). These patterns exhibit a superposition of two modes with different wavelengths. This is also identified in the corresponding DFT analysis results. In particular, we observe that the post-buckling pattern corresponding to $\eta = 1.7$ in Fig. 6 is not a typical wavy chain, but is composed of wavelets of small length scales (see the blue inclusion chains) enveloped in longer waves (see the red envelope curves). Correspondingly, we observe *two peaks* emerging in the DFT result after the onset of instability. The first peak locates at $k = 0.0625$ (representing the wavenumber of the envelope waves in large length scales), and the second peak locates at $k = 0.3125$ (representing the wavenumber of the wavelets in small length scales). Compared with the Bloch-Floquet prediction, $k^{cr} = 0.31$, the second peak in the post-buckling DFT analysis ($k = 0.3125$) represents the initial instability mode, and the first peak ($k = 0.0625$) represents an inclusion set in large length scales combined with the initial one for adaption of the composite configuration as the initial instability mode does not correspond to an integer number of initial primitive cells.

A further increase in the periodicity aspect ratio (see the pattern corresponding to $\eta = 1.9$ in Fig. 6) leads to the formation of seemingly disordered and lacking periodicity microstructures in the post-buckling regime. In the DFT results, a single peak is observed at $k = 0.4125$. However, this wavenumber is found to be larger than the prediction from the Bloch-Floquet analysis ($k^{cr} = 0.343$). This discrepancy results

from the limited number of inclusions that need to be accommodated (between 2 and 3, given $l^{cr} \approx 2.91$) in an enlarged primitive cell. The frustrated composite cannot transform into a periodic structure within the instability-dictated length scale, and hence, it is forced to conform with a combination of inclusion sets in different length scales. This adaptation in post-buckling development leads to the critical wavenumber diverging from its Bloch-Floquet prediction. The frustrated patterns, however, become more regulated as the periodicity aspect ratio further increases (see the pattern corresponding to $\eta = 2.0$ and $\eta = 2.1$ in Fig. 6). These composites start developing the periodicity doubling post-buckling structure (corresponding to a major peak at $k = 0.5$ in the DFT analysis) even though their critical wavenumber is not exactly 0.5. For example, the DFT analysis for the composite with $\eta = 2.0$ (see Fig. 6), shows the peak at $k = 0.5$, while the Bloch-Floquet prediction is $k^{cr} = 0.423$. Interestingly, for those composites attaining the periodicity-doubling mode, a single localized defect emerges (see Fig. 6 corresponding to $\eta = 2.0$). The DFT analysis also detects certain signals near the peak at $k = 0.5$. For instance, the DFT result corresponding to $\eta = 2.0$ in Fig. 6 detects multiple "minor signals" appears near the major peak at $k = 0.5$. These defects, however, disappear as the critical wavenumber is further increased. For example, the composite with $\eta = 2.1$ (corresponding to $k^{cr} = 0.455$ in the Bloch-Floquet analysis) exhibits a perfect periodicity doubling without developing the defects in the post-buckling regime. Finally, after the periodicity aspect

ratio reaches $\eta = 2.18$, the post-buckling pattern does not change with a further increase in the periodicity aspect ratio η, and the composite develops the exact periodicity-doubling in the post-buckling regime.

Next, we summarize the results of the post-buckling pattern developments as a map in the geometrical parameter space of η and ξ in Fig. 7. The map is divided into five sub-domains: (i) the red surface with diagonal strips – labeled as the "zigzag chain" – denotes the geometries for which longwave instabilities develop (with $k^{cr} \rightarrow 0$), where the post buckling pattern is a single zigzag chain of inclusions; (ii) the blue surface with diagonal strips – labeled as the "periodicity doubling" – denotes the microscopic instabilities with constant critical wavenumber $k^{cr} = 0.5$, and the post buckling pattern is the initial inclusion column being (exactly) doubled upon bifurcation; (iii) the solid pink surface – labeled with "Wavy chain" – denotes the microscopic instabilities with relatively low k^{cr} from 0 to the vicinity of 0.25, where the post-buckling pattern is a "wavy chain" of inclusions; (iv) the pure purple surface – labeled with "Superposed" – denotes the microscopic instabilities with relatively high k^{cr} from approximately 0.25 to 0.4, where the post-buckling pattern exhibits a superposition of wavelets (in small length scales) in between envelopes in large length scales; (v) the pure blue surface – labeled with "adapted periodicity doubling" – denotes the microscopic instabilities with k^{cr} close but not equal to 0.5; these composites adapt the "periodicity-doubling" post-buckling structure even though their critical wavenumber is not exactly 0.5.

While the post-buckling patterns demonstrate a good agreement with the Bloch-Floquet predictions [10] for small critical wavenumbers (typically, $k^{cr} \leq 0.5$), the difference appears when the critical wavenumber increases beyond $k^{cr} = 0.25$ (but not yet reached 0.5). The reason is that the composite configuration cannot transform into a periodic structure dedicated by the critical instability wavelength; the pattern is then forced to adapt a structure in nearby length scales, or a combination of inclusion sets in different length scales in the post-buckling regime. The formation of those adapted patterns necessitates a large enough finite deformation after the onset of instability; thus, it was not able to be shown in the Bloch-Floquet analysis that considers linearized incremental deformations (superposed upon the deformed state at the onset of instability). The post-buckling computations, together with the DFT analysis, capture those adapted post-buckling patterns with combined instability modes, enriching the understanding of the buckling behavior of particulate composites.

4.3. Evolution of post-buckling patterns upon further deformations

Finally, we examine the evolution of the post-buckling development with deformation beyond the critical loading. Here, we are specifically interested in the situation when the initial buckling mode changes with the applied deformation. Recall that the composites that develop relatively short-wave instability ($l^{cr} \lesssim 4$) are characterized by the adaptation of a combination of inclusion sets in different length scales in the post-buckling regime. Interestingly, in the post-buckling regime, we find the composite with a critical wavenumber lower than 0.25 (which initially forms a wavy-chain pattern) may also transform into a "superposed pattern" as the applied deformation forces the initial wavy buckling pattern to evolve. In Fig. 8, we illustrate this phenomenon via an example case for the composite with spacing ratio $\xi = 0.45$ and periodicity aspect ratio $\eta = 1.5$. The lower part of Fig. 8 shows the post-buckling pattern of the composite (illustrated by the inclusion center positions) right after the critical strain $\varepsilon^{cr} = 0.338$, and further after the buckling at $\varepsilon = 0.3386$, $\varepsilon = 0.34$ and $\varepsilon = 0.348$. The upper part of Fig. 8 shows the DFT analysis results corresponding to the above four deformation levels.

After the onset of instability at $\varepsilon^{cr} = 0.338$, the initial straight column of inclusions collapses and then transforms into a wavy chain as the compression continues to increase in a relatively small range. This is illustrated by the pattern in Fig. 8-2 showing the configuration at $\varepsilon = 0.3386$; the inclusions are located on a wavy curve with seemingly constraint amplitudes. The corresponding DFT results show a single peak at $k_I^{cr} = 0.15$. However, the corresponding wavelength $l_I^{cr} \approx 6.67$ is a non-integer value (see the DFT results corresponding to Fig. 8-2).

A further increase in the compressive strain leads to the transformation of the initial wavy chain pattern into a zigzag chain pattern. This emerging zigzag chain pattern appears to be enveloped between wavy curves in large length scales corresponding to the height of approximately 20 unit cells (see, for example, the area enveloped by the red dash curves in Fig. 8-4 corresponding to $\varepsilon = 0.348$). Interestingly, at the same time, we observe that there is a second peak in the Fourier coefficient emerging at $k_{II}^{cr} = 0.05$, indicating the existence of the envelope in large length scales. This two-peak DFT result was also observed in the post-buckling pattern shown in Fig. 6, corresponding to high wavenumbers ($k^{cr} > 0.25$). However, the case shown in Fig. 8 has a lower wavenumber $k_I^{cr} = 0.15$, and the first and second peak of the DFT results do not emerge simultaneously upon the onset of instability (the secondary peak emerges only after certain additional compression is
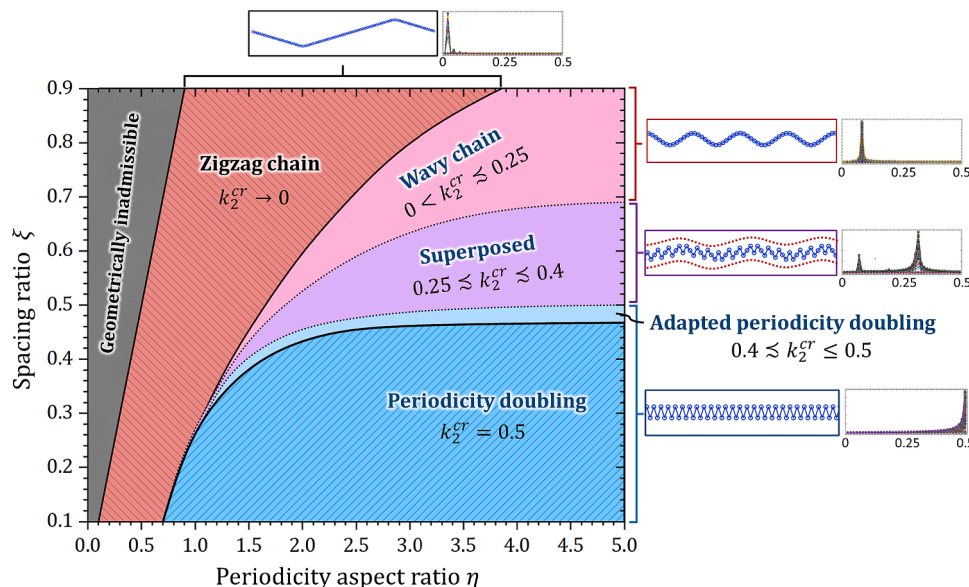

Fig. 7. Post-buckling pattern mapping in the geometrical parameter space.
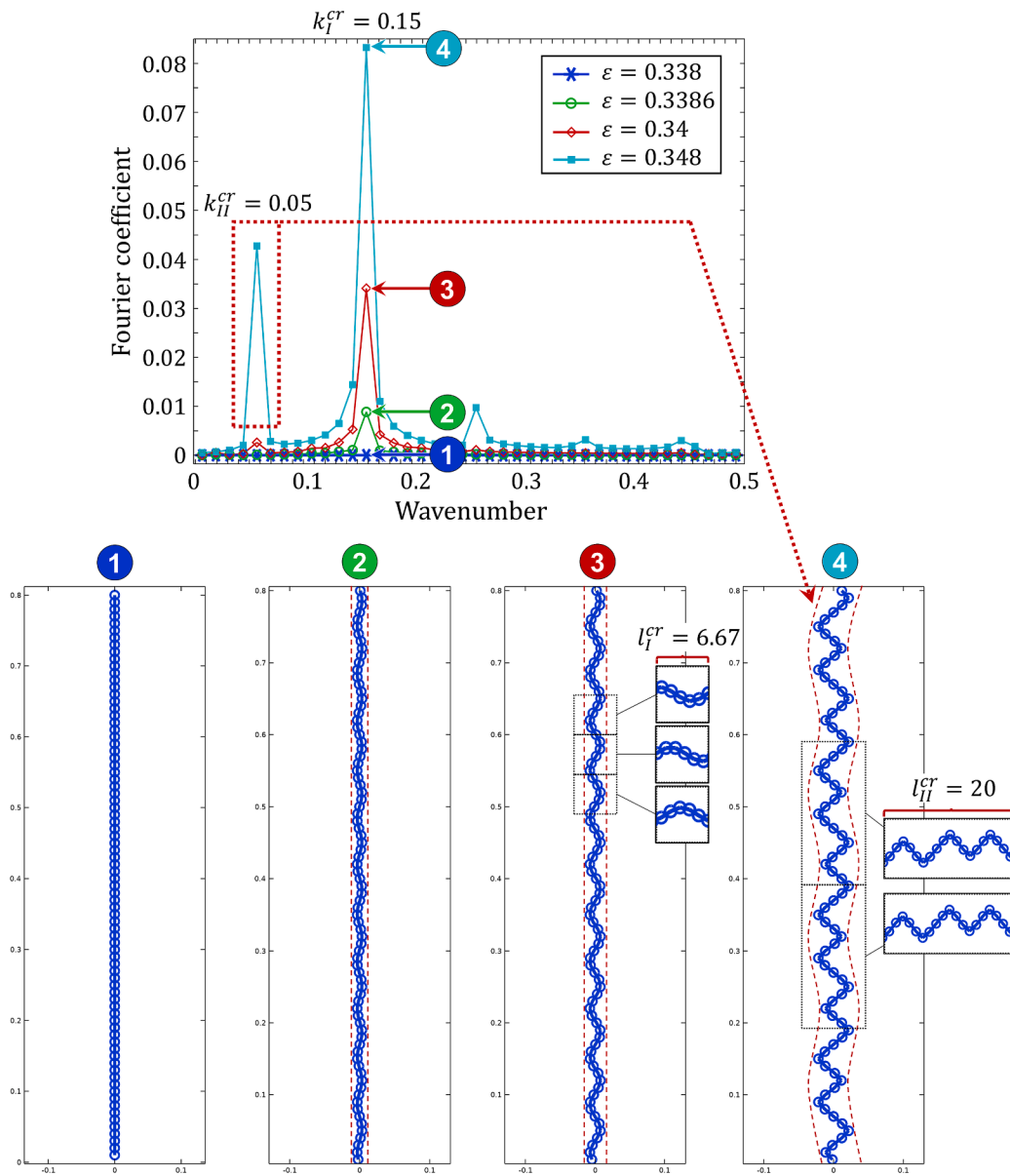
Fig. 8. Post-buckling patterns and the corresponding DFT results for the case with spacing ratio $\xi = 0.45$ and periodicity aspect ratio $\eta = 1.5$ under various compressive strain levels (1) $\varepsilon^{cr} = 0.338$, (2) $\varepsilon = 0.3386$, (3) $\varepsilon = 0.34$ and (4) $\varepsilon = 0.348$.

applied, while the first peak appears right after buckling). This is due to the fact that the initial wavy chain pattern (corresponding to the "first" wavenumber $k_I^{cr} = 0.15$, and the "first" critical wavelength $l_I^{cr} \approx 6.67$) does not have an integer number of inclusions in a wave period. For example, the inclusion blocks shown on the left of Fig. 8-3 exhibit seemingly incomplete wave periods with a non-integer number of inclusions between 5 and 6. Under relatively small increases in deformation after buckling, the inclusion chain can still maintain the overall wavy shape. However, as the post-buckling deformations become even higher, the composite can no longer maintain a non-integer number of inclusions in a wave period. It finally accommodates a combination of inclusion sets in different length scales. For example, the inclusion blocks shown on the right side of Fig. 8-4 have exactly 20 inclusions corresponding to the secondary critical wavelength $l_{II}^{cr} \approx 20$; and in each inclusion block we observe three small wavelets, the average length is $20/3 \approx 6.67$, which corresponds to the first critical wavelength $l_I^{cr} \approx 6.67$. The results discussed above indicate that the post-buckling pattern continues to evolve with further deformation after its initial formation. Remarkably, the evolution may be rather complex beyond a

simple amplification of the initial pattern. Specifically, the post-buckling pattern can evolve from a single wavy chain into distinct configurations characterized by a combination of inclusion sets with different length scales.

5. Conclusion

We have investigated the post-buckling development of instability-induced patterns in soft particulate composites. The collapse of the initial straight columns of inclusions in the particulate composites beyond the critical strain level, is followed by the formation of various post-buckling patterns: i) the "wavy-chain" of inclusions, ii) the "zigzag-chain" of inclusions, ii) the "periodicity doubling" pattern and iv) the "superposed" pattern (a combination of inclusion sets in different length scales), determined by the initial composite geometry. The onset of instability detected in post-buckling analysis agrees well with the critical strain predicted by the linearized Bloch-Floquet analysis superimposed on large deformation.

For the composites with instability modes characterized by a non-

integer number of inclusions in one wave period, the mismatch of inclusions in different wave periods occurs. To analyze the effect, we have developed a post-processing method based on the discrete Fourier transformation (DFT). The method is further used to characterize the post-buckling pattern and determine the critical wavenumber. The post-buckling patterns can then be quantified through the wavenumber spectrum obtained from the DFT analysis. In particular, the "zigzag-chain," "periodicity doubling," and "wavy-chain" patterns exhibit a single peak in the DFT spectrum with the fundamental wavenumber ($k = 1/N$), $k = 0.5$, and the intermediate wavenumber $1/N < k < 0.5$, respectively. The "superposed pattern" exhibit *double peaks* emerging in the corresponding DFT spectrum; here, one peak corresponds to the critical instability mode, and the other peak corresponds to an inclusion set of a large length scale. The two-peak spectrum indicates the adaption of the post-buckling pattern, as the composites cannot transform into the periodic structure dictated by the critical instability mode.

Next, we have investigated the transition of post-buckling patterns with respect to variations in geometric parameters. We have observed transitions from a "zigzag-chain" pattern to a "periodicity-doubling" pattern with an increase in the periodicity aspect ratio (corresponding to an increase in the distance between inclusion columns). In particular, when inclusions are initially close to each other in the direction of compression, the transition is binary with no intermediate patterns; when inclusions are far away from each other in the direction of compression, a transition from "zigzag-chain" to "wavy-chain" patterns is observed, but it never reaches the "periodicity doubling" pattern. When inclusions have a moderate distance from each other in the direction of compression, a more diverse array of transition patterns was observed, including the "wavy chain" pattern corresponding to relatively low k^{cr} (from 0 to the vicinity of 0.25), the "superposed pattern"

corresponding to a relatively high k^{cr} (from approximately 0.25 to 0.4) and the *adapted* "periodicity-doubling" pattern corresponding to k^{cr} close (but not equal) to 0.5, where the composites adapt the "periodicity-doubling" post-buckling structure even though their critical wavenumber is not exactly 0.5.

Finally, we observed that the post-buckling pattern continues to evolve with further deformation after its initial formation. Remarkably, the evolution may be rather complex beyond a simple amplification of the initial pattern. Specifically, we observed an evolution of the post-buckling pattern from a single wavy chain into distinct configurations characterized by a combination of inclusion sets with different length scales. While we detected a single post-buckling pattern evolution only, there may be additional modes that transform into new patterns in the post-buckling regime.

Declaration of Competing Interest

Data availability

Data will be made available on request.

Acknowledgments

Appendix A. The average shear of the post-buckling development and the identification of critical strains

To identify the onset of instability, a method to detect the collapse of the inclusion column is developed. It was observed that the collapse of the vertical inclusion column could be identified by the inclination of the inclusion chain, which can also be computed by counting relative horizontal displacement between neighboring inclusions. Similar to the approach used in our DFT analysis, we first measured the horizontal position of the inclusion centers $\{x_k\} := x_1, x_2, x_3 \cdots, x_N$ in $\boldsymbol{e}_1$ direction. Then, the so-called "average shear" γ of the inclusion chain is calculated by computing the slopes (absolute value) of the connection lines between centers of neighboring inclusion and averaging all slope values. Specifically, the computation can be written as

$$\gamma = \frac{1}{N} \frac{1}{\lambda b} \left[\sum_{k=1}^{N-1} (|x_{k+1} - x_k|) + |x_1 - x_N| \right], \tag{8}$$

where x_k denotes the position of the center of the k th inclusion (I_k) in $\boldsymbol{e}_1$ direction, and N is the total number of inclusions in the RVE (in particular, $N = 80$ in this study). When the composite is stable, the inclusion column maintains a straight alignment; thus, the "average shear" γ is equal to zero. However, as the inclusion column begins to collapse at the onset of instability, the "average shear" γ will be detected as a non-zero positive value. In this study, we set a threshold value $\gamma^{th} = 10^{-4}$ and identify the lowest compressive strain level that leads to $\gamma > \gamma^{th}$ as the critical strain.

The "average shear" is also used to quantify the development of the post-buckling deformation. Note that, this quantification is employed as it is independent of the critical wavenumber and is only related to the compressive strain. For example, Fig. S1 (a)-(c) illustrates post-buckling patterns with the same "average shear" γ but different critical wavenumbers $k^{cr} = 0.125$, $k^{cr} = 0.25$ and $k^{cr} = 0.5$. Therefore, in sec. 4.2, the same "average shear" value is selected for the post-buckling patterns with different wavenumbers for comparison. This unified "average shear" is set to $\gamma = 0.12$ in our study, which is large enough for the post-buckling pattern formation and not so large as to reach the next stage of evolution in the post-buckling pattern (as discussed in sec. 4.3).
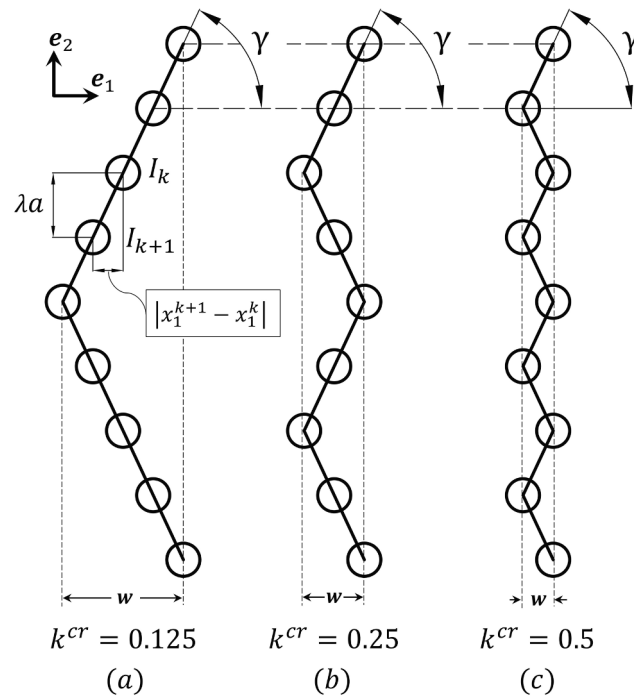
Fig. S1. The average shear of the post-buckling development.

For example, Fig. S2 shows the dependence of the "average shear" γ on the compressive strain for the composite with spacing ratio $\xi = 0.6$ and periodicity aspect ratio $\eta = 2.1$. We observe that the average shear γ starts with zero and suddenly increases beyond the threshold $\gamma = 10^{-3}$ after $\varepsilon = 0.2338$. Therefore, the critical strain is identified as $\varepsilon^{cr} = 0.2338$. Finally, the simulation stops at $\varepsilon = 0.24$ while γ reaches 0.12.
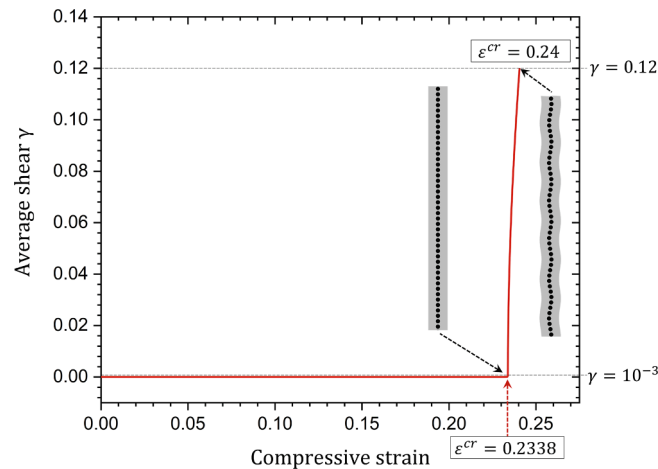

Fig. S2. The dependence of the average shear γ on the compressive strain for the composite with spacing ratio $\xi = 0.6$ and periodicity aspect ratio $\eta = 2.1$.

Appendix B. The influence of the number of unit cells in the RVE on the DFT analysis of post-buckling development

In this part, we show the influence of the number of unit cells (built in the RVE) on the DFT analysis results of the post-buckling development. We build multiple numerical models with different numbers of unit cells in the RVE (in particular, $N = 20, N = 40, N = 80, N = 120, N = 160$, and $N = 200$). The corresponding DFT results at the compressive strain level $\varepsilon = 0.237$ are shown in Fig. S3, where the Fourier coefficient of each curve is scaled so that their Fourier peak coefficients are all equal to one. We observe that as the number of unit cells N increases, the peak point of the curve slightly shifts and finally converges to $k^{cr} = 0.145$. A larger N can increase the precision of identifying the critical wavenumber since more wavenumbers are scanned. The results also show that $N = 80$ provides enough precision for the numerical simulation.
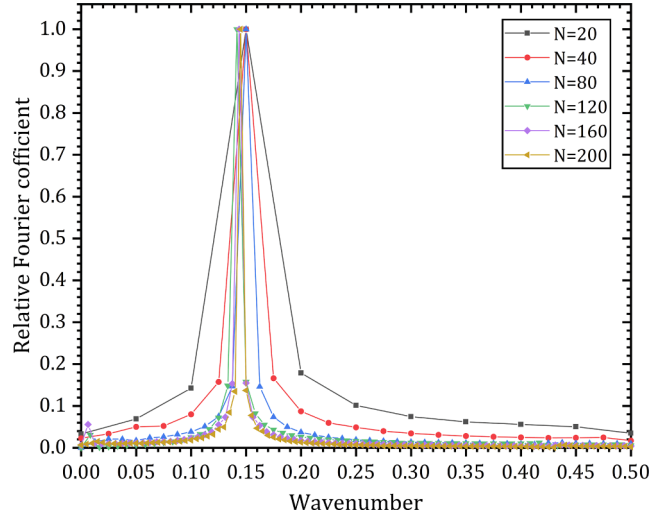
Fig. S3. The DFT results of the post-buckling development for composite with spacing ratio $\xi = 0.6$ and periodicity aspect ratio $\eta = 2.1$ at compressive strain $\varepsilon = 0.237$, for various numbers of unit cells built in the RVE ($N = 20, N = 40, N = 80, N = 120, N = 160$, and $N = 200$.).

Appendix C. Geometric imperfection.

As a perturbation to trigger instabilities, geometrical imperfection is introduced in terms of a slight alternation of the shape and position of the stiff inclusions. Specifically, as shown in Fig. S4, the inclusions are modeled as nearly-circular *ellipses*, where the geometrical differences are introduced independently onto the major diameter L_n, minor diameter S_n and the position X_n of the center of the n th inclusion, namely,

$$L_n = d + \Delta L_n,$$

$$S_n = d + \Delta S_n,$$

$$X_n = X + \Delta X_n.$$

where d is the diameter of the perfect circular inclusion and X_n is the acuate horizontal position of the center of the n th inclusion; ΔL_n, ΔS_n, and ΔX_n are random deviations. Note that the imperfections shown in Fig. S4(b) are significantly scaled for better illustration, since the original imperfection is too small to be visually discernible. Next, we generated three sets of random deviations,

$$\{\Delta L_n\} := \Delta L_1, \Delta L_2, \Delta L_3 \cdots, \Delta L_N,$$

$$\{\Delta S_n\} := \Delta S_1, \Delta S_2, \Delta S_3 \cdots, \Delta S_N,$$

$$\{\Delta X_n\} := \Delta X_1, \Delta X_2, \Delta X_3 \cdots, \Delta X_N,$$

and use them to alter the inclusions in the numerical model (where N is the total number of inclusions modeled in an RVE). Moreover, the distribution of the random set is symmetric to zero and is arranged to stay within $K_{imn} \bullet d$, where K_{imn} is the amplitude of deviation.
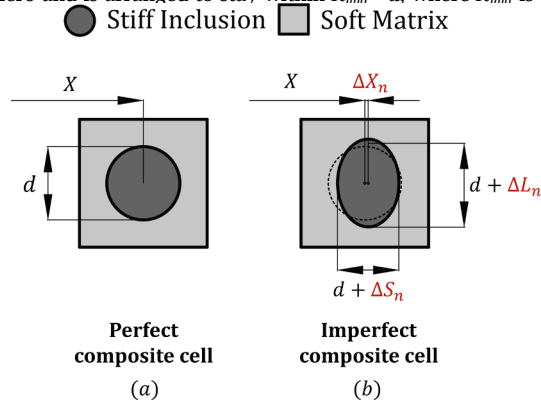

Fig. S4. (a) Schematic composite cell without geometric imperfection. (b) Schematic composite cell with geometric imperfections (the imperfections are significantly scaled in the figure for better illustration since the original imperfection is too small to be visually discernible).

To find the proper value of K_{imp} (with which the instabilities can be successfully triggered and the results are insensitive enough to the imperfections), we compare the results from numerical models with different K_{imp} (in particular, $K_{imp} = 10^{-2}, 10^{-3}, 10^{-4}, 10^{-5}, 10^{-6}$ and 10^{-7}). The corresponding DFT results are shown in Fig. S5(a) at the compressive strain level $\varepsilon = 0.241$ (after the Bloch-Floquet critical strain $\varepsilon^{cr} = 0.2338$). We observe that, for a large enough amplitude of deviation (for example, $K_{imp} = 10^{-2}, 10^{-3}, 10^{-4}$), the instability was successfully trigged. However, the inclusion chains (the post-buckling pattern) are found to be frustrated because of overwhelming imperfections, resulting in jagged DFT curves. For

small enough amplitudes of deviation (for example, $K_{imp} = 10^{-6}$ and 10^{-7}), the imperfection is too small that it fails to trigger the instability in numerical computation; thus, we find the DFT results maintain a zero line.
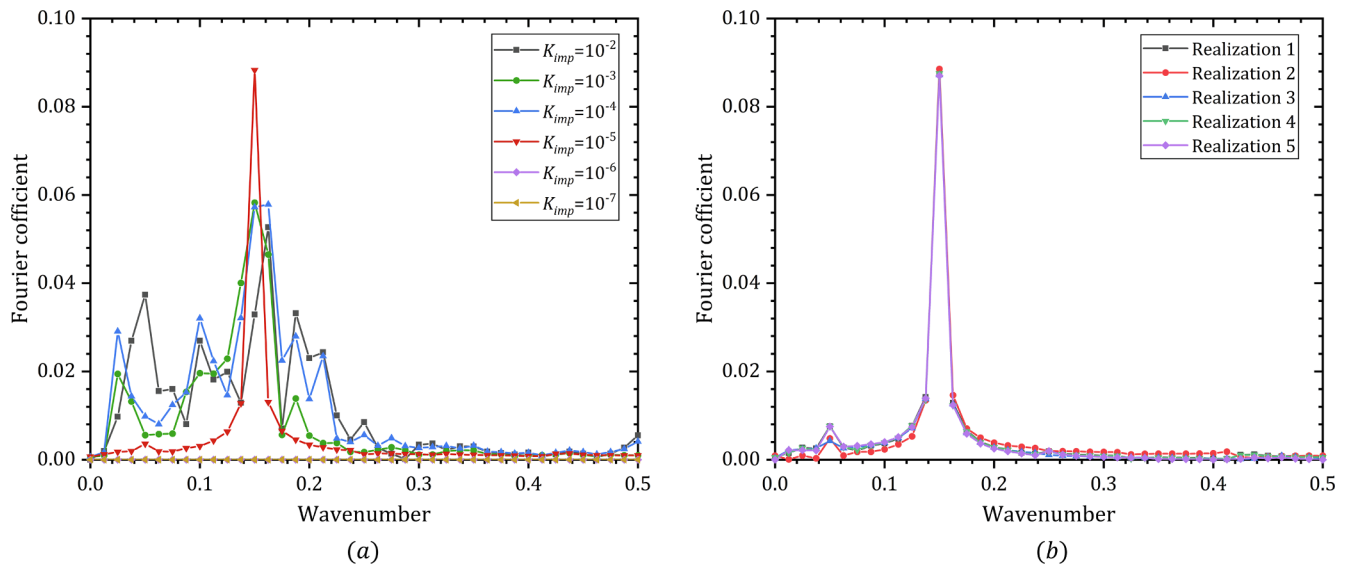
Fig. S5. The DFT results of the post-buckling development at compressive strain $\varepsilon = 0.241$ for numerical models with (a) various amplitudes of geometric imperfection ($K_{imp} = 10^{-2}, 10^{-3}, 10^{-4}, 10^{-5}, 10^{-5}$, and 10^{-7}); (b) different realizations of random imperfection with the same amplitude of geometric imperfection $K_{imp} = 10^{-5}$.

Our results indicate that, with an intermediate amplitude of deviation, $K_{imp} = 10^{-5}$, the instability pattern can be successfully triggered without being overwhelmed by the imperfections (see the red curve shown in Fig. S5(a) corresponding to $K_{imp} = 10^{-5}$). Moreover, to verify the insensitivity of the FEA results to specific realizations of the random imperfection, we compared five numerical models with independent realizations. The corresponding DFT results (where the peak corresponds to the critical wavenumber) are shown in Fig. S5(b). Moreover, the derived critical strains corresponding to realizations 1 to 5 are found at $\varepsilon^{cr} = 0.23377, 0.23374, 0.23375, 0.23377$, and 0.23378. These results demonstrate that, with an amplitude of deviation at $K_{imp} = 10^{-5}$, the critical strains and wavenumbers are insensitive enough to specific realizations of the random imperfection.

It should be noted that the imperfections introduced in our study are designed to trigger the instability without impacting the prediction of the composite's buckling behavior. However, they may not accurately reflect the imperfections in natural materials resulting from geometrical [9,12,57] or material [22,23,45] uncertainties. The prediction of the composite's buckling behavior may be affected by those uncertainties. Additionally, interphases between the composite constituents, which may occur during the material manufacturing processes, can potentially affect the instability characteristics [1]. To quantify the influence of these uncertainties, multi-field coupled stochastic analyses can be employed [14,32].

Appendix D. Additional Details of Finite Element Analysis (FEA)

This section provides additional details of the FEA computation of post-bucking in particulate composites using COMSOL Multiphysics 6.0. The 2D geometric model was constructed using the software's built-in Geometry module. The model mesh is generated with 2D quads elements (9-node) with quadratic Lagrange shape function. The mesh was particularly refined near the interface between the soft and stiff material phases, resulting in a minimum element size of $10^{-2}b$ and a maximum element size of $5 \bullet 10^{-2}b$ (where b is the length of a single primitive unit cell). We assign pure hyperelastic models to both stiff inclusion and soft matrix materials without rate-dependent properties. Moreover, the mechanical loading was applied quasi-statically, which ignores the materials' mass effect. Finally, we performed convergence studies to ensure the insensitivity of the FEA results to the mesh quality, as well as the validation of the accuracy and reliability of the simulation.

References

[1] Arora N, Batan A, Li J, Slesarenko V, Rudykh S. On the influence of inhomogeneous interphase layers on instabilities in hyperelastic composites. Materials 2019;12(5).

[2] Arora N, Yao Q, Rudykh S. Deformation activated negative group velocity state in soft laminates. Extreme Mech Lett 2022;51:101592.

[3] Arora N, Li J, Rudykh S. Tunable buckling configurations via in-plane periodicity in soft 3D-fiber composites: Simulations and experiments. Int J Solids Struct 2022; 250.

[4] Aboudi J, Volokh KY. Modeling deformation and failure of viscoelastic composites at finite strains. Mech Soft Mater 2020;2:1–19.

[5] Aboudi J, Gilat R. Bifurcation buckling and the effect of imperfections on the microbuckling of soft materials with periodic microstructure by the finite strain HFGMC micromechanics. Int J Solids Struct 2023;270:112227.

[6] Bertoldi K, Boyce MC, Deschanel S, Prange SM, Mullin T. Mechanics of deformation-triggered pattern transformations and superelastic behavior in periodic elastomeric structures. J Mech Phys Solids 2008;56(8):2642–68.

[7] Bruno D, Greco F, Lonetti P, Blasi PN, Sgambitterra G. An investigation on microscopic and macroscopic stability phenomena of composite solids with periodic microstructure. Int J Solids Struct 2010;47(20):2806–24.

[8] Bertoldi K, Reis PM, Willshaw S, Mullin T. Negative Poisson's ratio behavior induced by an elastic instability. Adv Mater 2010;22(3):361–6. https://doi.org/10.1002/adma.200901956.

[9] Chen LL, Lian H, Liu Z, Chen HB, Atroshchenko E, Bordas SPA. Structural shape optimization of three dimensional acoustic problems with isogeometric boundary element methods. Comput Methods Appl Mech Eng 2019;355:926–51.

[10] Chen D, Arora N, Xiang Y, Li J, Slesarenko V, Rudykh S. Instability-induced patterns and their post-buckling development in soft particulate composites. Mech Mater 2022;175:104482.

[11] De Maio U, Greco F, Luciano R, Sgambitterra G, Pranno A. Microstructural design for elastic wave attenuation in 3D printed nacre-like bioinspired metamaterials lightened with hollow platelets. Mech Res Commun 2023;104045.

[12] Ding C, Deokar RR, Ding Y, Li G, Cui X, Tamma KK, et al. Model order reduction accelerated Monte Carlo stochastic isogeometric method for the analysis of structures with high-dimensional and independent material uncertainties. Comput Methods Appl Mech Eng 2019;349:266–84.

[13] Ehret AE, Itskov M. A polyconvex hyperelastic model for fiber-reinforced materials in application to soft tissues. J Mater Sci 2007;42:8853–63.

[14] Elouneg A, Sutula D, Chambert J, Lejeune A, Bordas SPA, Jacquet E. An open-source FEniCS-based framework for hyperelastic parameter estimation from noisy full-field data: Application to heterogeneous soft tissues. Comput Struct 2021;255.

[15] Galich PI, Slesarenko V, Li J, Rudykh S. Elastic instabilities and shear waves in hyperelastic composites with various periodic fiber arrangements. Int J Eng Sci 2018;130:51–61.

[16] Geymonat G, Müller S, Triantafyllidis N. Homogenization of nonlinearly elastic materials, microscopic bifurcation and macroscopic loss of rank-one convexity. Arch Ration Mech Anal 1993;122(3):231–90.

[17] Greco F, Leonetti L, De Maio U, Rudykh S, Pranno A. Macro- and micro-instabilities in incompressible bioinspired composite materials with nacre-like microstructure. Compos Struct 2021;269.

[18] Greco F, Lonetti P, Luciano R, Blasi PN, Pranno A. Nonlinear effects in fracture induced failure of compressively loaded fiber reinforced composites. Compos Struct 2018;189:688–99.

[19] Greco F, Luciano R. A theoretical and numerical stability analysis for composite micro-structures by using homogenization theory. Compos B Eng 2011;42(3):382–401.

[20] Goshkoderia A, Chen V, Li J, Juhl A, Buskohl P, Rudykh S. Instability-Induced Pattern Formations in Soft Magnetoactive Composites. Phys Rev Lett 2020;124(15):1–7.

[21] Gao N, Li J, Bao RH, Chen WQ. Harnessing uniaxial tension to tune Poisson's ratio and wave propagation in soft porous phononic crystals: an experimental study. Soft Matter 2019;15(14):2921–7.

[22] Hauseux P, Hale JS, Bordas SPA. Accelerating Monte Carlo estimation with derivatives of high-level finite element models. Comput Methods Appl Mech Eng 2017;318:917–36.

[23] Hauseux P, Hale JS, Cotin S, Bordas SPA. Quantifying the uncertainty in a hyperelastic soft tissue model with stochastic parameters. App Math Model 2018;62:86–102.

[24] Li J, Pallicity TD, Slesarenko V, Goshkoderia A, Rudykh S. Domain formations and pattern transitions via instabilities in soft heterogeneous materials. Adv Mater 2019;31(14):1807309.

[25] Li J, Rudykh S. Tunable microstructure transformations and auxetic behavior in 3D-printed multiphase composites: The role of inclusion distribution. Compos B Eng 2019;172:352–62.

[26] Li J, Wang Y, Chen W, Wang YS, Bao R. Harnessing inclusions to tune post-buckling deformation and bandgaps of soft porous periodic structures. J Sound Vib 2019;459:114848.

[27] Li J, Slesarenko V, Galich PI, Rudykh S. Instabilities and pattern formations in 3D-printed deformable fiber composites. Compos B Eng 2018;148:114–22.

[28] Li J, Slesarenko V, Rudykh S. Auxetic multiphase soft composite material design through instabilities with application for acoustic metamaterials. Soft Matter 2018;14(30):6171–80.

[29] Li J, Slesarenko V, Rudykh S. Microscopic instabilities and elastic wave propagation in finitely deformed laminates with compressible hyperelastic phases. Eur J Mech, A/Solids 2019;73:126–36.

[30] Li J, Slesarenko V, Rudykh S. Emergence of instability-driven domains in soft stratified materials. npj Comput Mater 2022;8(1):100.

[31] Li Y, Kaynia N, Rudykh S, Boyce MC. Wrinkling of interfacial layers in stratified composites. Adv Eng Mater 2013;15(10):921–6.

[32] Mazier A, Bilger A, Forte AE, Peterlik I, Hale JS, Bordas SPA. Inverse deformation analysis: an experimental and numerical assessment using the FEniCS Project. Eng Comput 2022.

[33] Merodio J, Pence TJ. Kink surfaces in a directionally reinforced neo-Hookean material under plane deformation: I. Mechanical equilibrium. J Elast 2001;62:119–44.

[34] Merodio J, Pence TJ. Kink surfaces in a directionally reinforced neo-Hookean material under plane deformation: II. Kink band stability and maximally dissipative band broadening. J Elast 2001;62:145–70.

[35] Merodio J, Ogden RW. Material instabilities in fiber-reinforced nonlinearly elastic solids under plane deformation. Arch Mech 2002;54(5–6):525–52.

[36] Merodio J, Ogden RW. Instabilities and loss of ellipticity in fiber-reinforced compressible non-linearly elastic solids under plane deformation. Int J Solids Struct 2003;40(18):4707–27.

[37] Merodio J, Ogden RW. Remarks on instabilities and ellipticity for a fiber-reinforced compressible nonlinearly elastic solid under plane deformation. Q Appl Math 2005;63(2):325–33.

[38] Merodio J, Ogden RW. Tensile instabilities and ellipticity in fiber-reinforced compressible non-linearly elastic solids. Int J Eng Sci 2005;43(8–9):697–706.

[39] Melnikov A, Ogden RW, Dorfmann L, Merodio J. Bifurcation analysis of elastic residually-stressed circular cylindrical tubes. Int J Solids Struct 2021;226–227:111062.

[40] Mullin T, Deschanel S, Bertoldi K, Boyce MC. Pattern transformation triggered by deformation. Phys Rev Lett 2007;99(8).

[41] Michel JC, Lopez-Pamies O, Ponte Castaeda P, Triantafyllidis N. Microscopic and macroscopic instabilities in finitely strained fiber-reinforced elastomers. J Mech Phys Solids 2010;58(11):1776–803.

[42] Ogden RW. Non-linear elastic deformations. Mineola, New York: Dover Publication; 1997.

[43] Qiu GY, Pence TJ. Loss of ellipticity in plane deformation of a simple directionally reinforced incompressible nonlinearly elastic solid. J Elast 1997;49:31–63.

[44] Pranno A, Greco F, Leonetti L, Lonetti P, Luciano R, De Maio U. Band gap tuning through microscopic instabilities of compressively loaded lightened nacre-like composite metamaterials. Compos Struct 2022;282:115032.

[45] Rappel H, Beex LAA, Noels L, Bordas SPA. Identifying elastoplastic parameters with Bayes' theorem considering output error, input error and model uncertainty. Probab Eng Mech 2019;55:28–41.

[46] Rudykh S, Boyce MC. Transforming wave propagation in layered media via instability-induced interfacial wrinkling. Phys Rev Lett 2014;112(3).

[47] Rudykh S, Debotton G. Instabilities of hyperelastic fiber composites: Micromechanical versus numerical analyses. J Elast 2012;106(2):123–47.

[48] Shan S, Kang SH, Wang P, Qu C, Shian S, Chen ER, et al. Harnessing Multiple Folding Mechanisms in Soft Periodic Structures for Tunable Control of Elastic Waves. Adv Funct Mater 2014;24(31):4935–42.

[49] Slesarenko V, Rudykh S. Harnessing viscoelasticity and instabilities for tuning wavy patterns in soft layered composites. Soft Matter 2016;12(16):3677–82.

[50] Slesarenko V, Rudykh S. Microscopic and macroscopic instabilities in hyperelastic fiber composites. J Mech Phys Solids 2017;99:471–82.

[51] Slesarenko V, Galich PI, Li J, Fang NX, Rudykh S. Foreshadowing elastic instabilities by negative group velocity in soft composites. Appl Phys Lett 2018;113(3).

[52] Triantafyllidis N, Nestorović MD, Schraad MW. Failure Surfaces for Finitely Strained Two-Phase Periodic Solids Under General In-Plane Loading. J Appl Mech 2006;73(3):505–15.

[53] Volokh KY. Loss of ellipticity in elasticity with energy limiters. Eur J Mech-A/Solids 2017;63:36–42.

[54] Wang P, Casadei F, Shan S, Weaver JC, Bertoldi K. Harnessing Buckling to Design Tunable Locally Resonant Acoustic Metamaterials. Phys Rev Lett 2014;113(1):014301.

[55] Xiang Y, Schilling C, Arora N, Boydston AJ, Rudykh S. Mechanical characterization and constitutive modeling of visco-hyperelasticity of photocured polymers. Addit Manuf 2020;36:101511.

[56] Xiang Y, Zhong D, Rudykh S, Zhou H, Qu S, Yang W. A Review of Physically Based and Thermodynamically Based Constitutive Models for Soft Materials. J Appl Mech, Trans ASME 2020;87(11):110801.

[57] Yu P, Bordas SPA, Kerfriden P. Adaptive Isogeometric analysis for transient dynamics: Space–time refinement based on hierarchical a-posteriori error estimations. Comput Methods Appl Mech Eng 2022;394:114774.